

Article

Microstructural Evolution from Dendrites to Core-Shell Equiaxed Grain Morphology for CoCrFeNiV_x High-Entropy Alloys in Metallic Casting Mold

Leigang Cao , Lin Zhu, Hongde Shi, Zerui Wang, Yue Yang, Yi Meng, Leilei Zhang and Yan Cui *

Department of Materials Science and Engineering, North China University of Technology, Beijing 100144, China; zhulinych@hotmail.com (L.Z.); shd19971020@hotmail.com (H.S.); wangzerui1997@gmail.com (Z.W.); yyue@ncut.edu.cn (Y.Y.); mengyi@ncut.edu.cn (Y.M.); zhangleilei@ncut.edu.cn (L.Z.)

* Correspondence: caolg@ncut.edu.cn (L.C.); cuiyan@ncut.edu.cn (Y.C.);

Tel.: +86-10-8880-2105 (L.C.); +86-10-8880-3729 (Y.C.)

Received: 30 September 2019; Accepted: 29 October 2019; Published: 30 October 2019



Abstract: The CoCrFeNiV_x ($x = 0, 0.25, 0.5, 0.7, 0.8, 0.9,$ and 1.0) high-entropy alloys (HEAs) were fabricated by the copper mold casting process. The microstructure, phase constitution, and mechanical properties were investigated by using X-ray diffraction, scanning electron microscopy, transmission electron microscopy analyses and compressive testing. It revealed that, when $x \leq 0.25$, the alloys solidified into a single fcc phase. When $0.5 \leq x \leq 0.8$, the alloys solidified into a dendritic structure of the fcc phase with the formation of the σ phase in the interdendrite region. Interestingly, when x exceeded 0.9, the alloys presented a typical core-shell equiaxed grain morphology. The core region consisting of a mixture of fcc + σ phases was surrounded by the shell of the single σ phase and the interdendrite region solidified into the single fcc phase. The dual-phase “eutectoid” structure in the core region of the equiaxed grain might be formed from the decomposition of the unidentified metastable phase. As the V fraction increased, the compressive yield strength of the CoCrFeNiV_x alloys gradually increased from 164 MPa ($x = 0$) to 458 MPa ($x = 0.8$), and then sharply increased to 722 MPa ($x = 0.9$) and 1493 MPa ($x = 1.0$).

Keywords: high-entropy alloy; solidification; microstructure; sluggish diffusion

1. Introduction

Alloying is used as an effective route to improve the mechanical properties of structural metallic materials over the long term via well-established strengthening mechanisms such as solid-solution strengthening by inducing lattice distortion and precipitation strengthening with the formation of second phases with different properties [1–3]. Traditionally, researchers have mainly focused on the corners of a phase diagram for alloy design. It is because, according to the Gibbs phase rule [4], the complex element constitution usually gives rise to the increasing kinds and fraction of the addition phase (e.g., intermetallics). This will, in many cases, weaken the comprehensive mechanical properties. Conversely, it is interesting that multi-component alloys such as the fcc-type CoCrFeNiMn alloy [5], bcc-type AlCoCrFeNi alloy [6], hcp-type YGdTbDyLu alloy [7], or a mixture of them, are prone to form a simple phase constitution, instead of multi-phase constitution. The phenomenon is against the theoretical prediction. The early ground-breaking experiments of multi-component alloys with equal or near-equal elemental constituents were undertaken intermittently in 1981–2004 by Cantor et al. [4,8], Ranganathan [9], and Yeh et al. [9–11]. This kind of alloy system was termed by Yeh as the

widely accepted “high-entropy alloys (HEAs)”, which contains at least five metallic elements, with the composition of each element being 5–35 at.%.

Aside from their interesting solidification behaviors, high-entropy alloys also present great potential to be used as structural materials due to their excellent properties such as high hardness [12,13], high strength [14–16], good oxidation resistance [17], soft-magnetic properties [18], softening resistance at high temperature [3], and recently revealed, perfect irradiation resistance [19]. Considering the existence of dozens of metallic elements, this new type of alloy implies that a large number of new multi-component metallic materials with excellent properties, which was neglected previously, might be fabricated to serve humanity. Therefore, high-entropy alloys have become a hot topic in materials science. In the past 15 years, many investigations have been performed to study the fundamental feature of multi-component HEAs and many valuable achievements have been obtained. First, the variation of certain constitutional elements can strongly change the crystalline structure, microstructural morphology, and the subsequent mechanical properties. For example, the microstructure of the $\text{Al}_x\text{CoCrFeNi}$ system [20] presents a complex transition from a columnar cellular structure to dendritic grain structures as the Al composition is increased. Correspondingly, the fraction of the bcc phase is increased gradually and reaches 100% when x exceeds 0.9, giving rise to an increasing trend in the hardness. A similar variation trend of the crystalline structure and tensile strength was also found in $\text{Al}_x\text{CoCrFeNiMn}$ HEAs [1]. Recently, laser additive manufacturing provides a high-throughput characterization method to assess the effect of the element on the microstructure and properties of the HEAs by fabricating the compositionally graded HEAs [21–23]. The designed composition gradient can give rise to the continuous change of the mechanical properties of the alloy, which can also be used as an approach for surface treatment or gradient materials. Furthermore, some effective approaches that are usually used in traditional metallic materials can also be adopted to strengthen the HEAs. For example, He et al. [15] successfully developed the $(\text{CoCrFeNi})_{94}\text{Ti}_2\text{Al}_4$ alloys with enhanced tensile properties by incorporating the nanosized coherent reinforcing $\text{L}_{12}\text{-Ni}_3(\text{Ni, Al})$ precipitates. As a consequence, the yield strength, tensile strength, and plasticity of the water-quenched alloys after (1) cold rolling (30%), annealing (1273 K + 2 h), and aging (1073 K + 18 h), and (2) cold rolling (70%) and aging (973 K + 2 h), could be improved to 645 MPa, 1094 MPa, and 39% and 1005 MPa, 1272 MPa, and 17%, respectively. In comparison, the tensile strength and plasticity of the as-homogenized control sample were only about 503 MPa and 68%, respectively. Gludovatz et al. [24] successfully prepared a grain refined CoCrMnFeNi alloy with an $\sim 6 \mu\text{m}$ grain by cold forging, cross rolling, and full recrystallization. The prepared alloy presents excellent mechanical properties even in cryogenic conditions. In addition, the transformation-induced plasticity (TRIP) effect, which has been developed to improve the plasticity of the steels, titanium alloys [25], and amorphous alloys [26], has also been successfully introduced into the $\text{Fe}_{50}\text{Mn}_{30}\text{Cr}_{10}\text{Co}_{10}$ [27] and TaHfZrTi [28] HEAs.

It seems that many obvious improvements can be achieved in the increase of the mechanical properties of the HEAs by means of the processing techniques. However, we must realize that the fabricating process is actually based on the microstructure and phase constitution of the as-solidified alloys, namely that the feature of the as-solidified HEAs is rather important for either direct use as structural materials or for further modification of the mechanical property by subsequent processing techniques like rolling and heat treatment. Therefore, it is still necessary to experimentally investigate the alloying effects on the microstructure evolution and phase selection, and their effects on the subsequent mechanical properties, especially under the condition of lack of the thermodynamic phase diagram. In addition to bcc and hcp precipitates, the tetragonal phase can also be an effective reinforcing phase in fcc-matrix HEAs with the addition of the additional component. One such is the equal-atomic five-component CoCrFeNiV alloy [29], the strength of which could be strongly enhanced by the formation of the σ phase with dramatic loss of the plasticity. Conversely, equal-atomic four-component CoCrFeNi alloy usually solidified into a typical fcc structure with excellent plasticity, but low strength [20,30]. This indicates that the comprehensive mechanical properties of the CoCrFeNi alloy could be improved by controlling the fraction and distribution of the σ phase reinforcement

as the V content is increased. However, the solidification behavior of the CoCrFeNiV_x HEAs with the V addition is still unclear. Therefore, in this study, as-cast CoCrFeNiV_x HEAs were fabricated by the copper mold casting method to investigate microstructure evolution, solidification behavior, and mechanical properties with the addition of the V element. The results can give access to understanding and controlling the fundamental solidification process of the CoCrFeNiV_x HEAs for the development of the high-performance materials.

2. Materials and Methods

CoCrFeNiV_x ($x = 0, 0.25, 0.5, 0.7, 0.8, 0.9,$ and 1.0) alloys were fabricated by an arc-melting furnace. The purity of raw materials was higher than 99.99 wt%. The furnace was pumped to a pressure of 2×10^{-3} Pa and then back-filled with Ar gas to a pressure of 1.5×10^3 Pa. Pure titanium ingot was melted first to remove the residual oxygen and oxygen-containing substance in the evacuated chamber, and then the alloys were arc-melted five times to ensure chemical homogeneity.

The arc-melted alloy was loaded into a quartz crucible with a hole (about 1 mm diameter) in the center of the base, which was then placed into a single roll melt-spinner. The top end of the crucible was connected with the high-pressure gas line. The copper roller for melt-spinning was removed and replaced by the copper mold. During the casting process, the crucible had two fixed working positions for melting and ejecting the liquid alloys. Therefore, before evacuating the chamber, the crucible was adjusted to the appropriate position to make sure that during the heating step, the section of the crucible with the alloy was surrounded by the radio-frequency (RF) coil and, during the ejecting step, the bottom of the crucible was right above the copper mold with the distance being about 0.3 mm. The system was then evacuated to a pressure of 3×10^{-3} Pa for induction heating. A reflective mirror, in line with the axis of the crucible, was fixed on the top of the instrument to determine the melting process of the alloy. Once the alloy was melted, the crucible was instantly dropped down to the “ejecting position” and the melt was rapidly ejected into the mold immediately with high-pressure argon. A series of cylindrical alloy rods with a diameter of 5 mm and a length of 10 mm were fabricated, as is shown in Figure 1.



Figure 1. The \varnothing 5 mm alloy rod solidified in the copper mold.

The cross-sections of all alloys were ground using SiC papers (320–2000 grit) for phase identification by X-ray diffractometer (XRD, Rigaku Ultimate-IV, Rigaku, Tokyo, Japan) with Cu K α radiation. The scans focused on the entire cross-section area of the casting rods using a continuous mode with a scan speed of 10 °/min. Then, the samples were mounted in conductive resin and polished using 2.5 μ m and 1 μ m diamond paste and 0.05 μ m alumina suspension (Buehler, Lake Bluff, IL, USA). The samples were washed manually using dilute detergent and by ultrasonic cleaning using an ethanol medium during each polishing step. The microstructure of the alloys (central region of the cross-section) and the average element composition of the alloys and the expected areas/phases were investigated using a backscattered electron detector (BSD) and an energy dispersive spectrometry detector (EDX, Bruker Quantax XFlash 6|60, Bruker, Berlin, Germany) mounted on a Zeiss sigma 300 scanning electron microscope (SEM, Carl Zeiss Ltd, Cambridge, UK) with an accelerating voltage of 15 kV. TEM analyses also focused on the central region of the cross-section for microstructure

observation and phase identification using a transmission electron microscope (TEM, FEI Tecnai G2 F30, FEI Co. Ltd, Hillsboro, OR, USA) with an accelerating voltage of 300 kV. The TEM specimen was fabricated by the ion milling of a disk-shaped foil with the thickness and diameter being about 30 μm and 5 mm, respectively, by using a Gatan 691 precision ion polishing system (Gatan, Pleasanton, CA, USA). XRD and TEM diffraction patterns were annotated for phase identification using the powder diffraction pattern file database (2014). Room-temperature compressive properties were performed on the cylindrical samples ($\varnothing 5 \times 10 \text{ mm}^2$) with a strain rate of $1 \times 10^{-3} \text{ s}^{-1}$. It should be ensured that there are no casting holes on the surface and cross section of the cylindrical samples. A compression test was carried out one time for the CoCrFeNiV_x ($x \leq 0.8$) alloys. For the $\text{V}_{0.9}$ and $\text{V}_{1.0}$ alloys, the fracture surface of the fragments after compression test was also checked and the test needs to be repeated if a casting hole is found.

3. Results and Discussion

3.1. Alloy Composition

The EDX measurements were carried out to confirm the compositions of the CoCrFeNiV_x alloys (denoted as V_x hereafter). The average composition of each alloy was determined by scanning at least 10 random areas of the cross-section with the rectangular scanning range of $500 \times 350 \mu\text{m}^2$ (Table 1). It is clear that the measured element compositions of the casting rods were almost the same as the expected values. It followed that the samples met the requirement of the experimental investigation.

Table 1. Average elemental composition of the CoCrFeNiV_x alloys measured by energy dispersive spectrometry analysis (EDX).

Alloy		Co/at.%	Cr/at.%	Fe/at.%	Ni/at.%	V/at.%
$\text{V}_{0.0}$	Nominal	25.00	25.00	25.00	25.00	-
	Measured	25.74 ± 0.20	24.97 ± 0.20	25.17 ± 0.19	24.12 ± 0.25	-
$\text{V}_{0.25}$	Nominal	23.53	23.53	23.53	23.53	5.88
	Measured	24.31 ± 0.26	23.47 ± 0.23	23.78 ± 0.36	22.75 ± 0.15	5.79 ± 0.07
$\text{V}_{0.5}$	Nominal	22.22	22.22	22.22	22.22	11.11
	Measured	22.92 ± 0.27	22.31 ± 0.22	22.38 ± 0.21	21.42 ± 0.32	10.95 ± 0.19
$\text{V}_{0.7}$	Nominal	21.28	21.28	21.28	21.28	14.89
	Measured	21.93 ± 0.25	21.26 ± 0.29	21.35 ± 0.14	20.67 ± 0.28	14.79 ± 0.14
$\text{V}_{0.8}$	Nominal	20.83	20.83	20.83	20.83	16.67
	Measured	21.46 ± 0.23	20.53 ± 0.26	21.02 ± 0.16	20.39 ± 0.25	16.60 ± 0.19
$\text{V}_{0.9}$	Nominal	20.41	20.41	20.41	20.41	18.37
	Measured	21.01 ± 0.24	20.35 ± 0.19	20.47 ± 0.20	19.93 ± 0.32	18.24 ± 0.18
$\text{V}_{1.0}$	Nominal	20.00	20.00	20.00	20.00	20.00
	Measured	20.71 ± 0.17	20.02 ± 0.17	20.09 ± 0.25	19.46 ± 0.23	19.72 ± 0.24

3.2. Microstructure Evolution

It was revealed by the SEM and TEM analyses that the microstructure of the alloys transformed from dendrite to an equiaxed structure morphology with the V addition, as shown in Figures 2–4. First, the V_0 and $\text{V}_{0.25}$ alloys present a single fcc phase, according to the SEM micrographs (Figure 2a,b) and the TEM images and diffraction patterns (Figure 2d,e,g,h). The formation of the additional σ phase was found in the $\text{V}_{0.5}$ alloy (Figure 2c). Then, the CoCrFeNiV_x with a high V content ($0.7 \leq x \leq 1.0$) presents a distinct transition of microstructure morphologies, although they possessed the same phase constitution of the fcc and σ phases. The $\text{V}_{0.7}$ and $\text{V}_{0.8}$ alloys displayed a typical dendrite structure of the fcc phase, with remaining liquid in the interdendritic region solidifying into the σ phase (Figure 3a,c). This indicates a simple solidification behavior of the dendrite growth of the fcc phase with the residual liquid in the interdendrite region forming the σ phase. A similar microstructural morphology was also observed in the copper-mold solidified $(\text{FeNiCoCu})_{95}\text{V}_5$ HEAs [31].

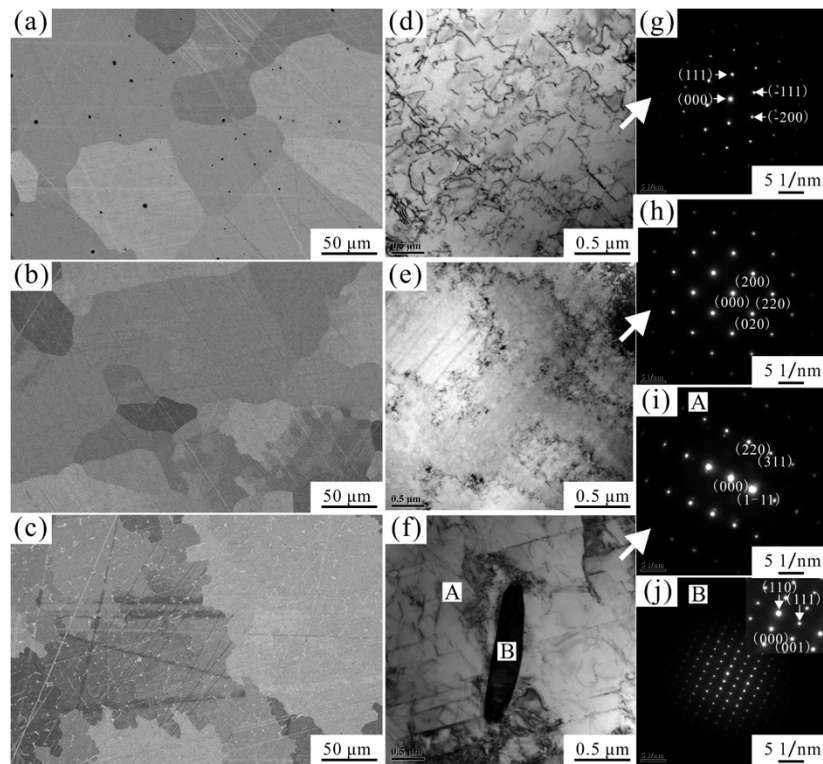


Figure 2. (a–c) SEM micrographs of the $V_{0.0}$, $V_{0.25}$, and $V_{0.5}$ rods, respectively. (d–f) TEM micrographs of the $V_{0.0}$, $V_{0.25}$ and $V_{0.5}$ rods, respectively. (g–j) TEM selected area diffraction patterns corresponding to (a), (b), and the phases marked as A and B in (f), respectively. The white flake phase that first formed in the $V_{0.5}$ alloy (c) was identified as the σ phase. The straight lines in (a–c) are the stretches and the black spots in (a) are the surface contaminants introduced during the polishing process.

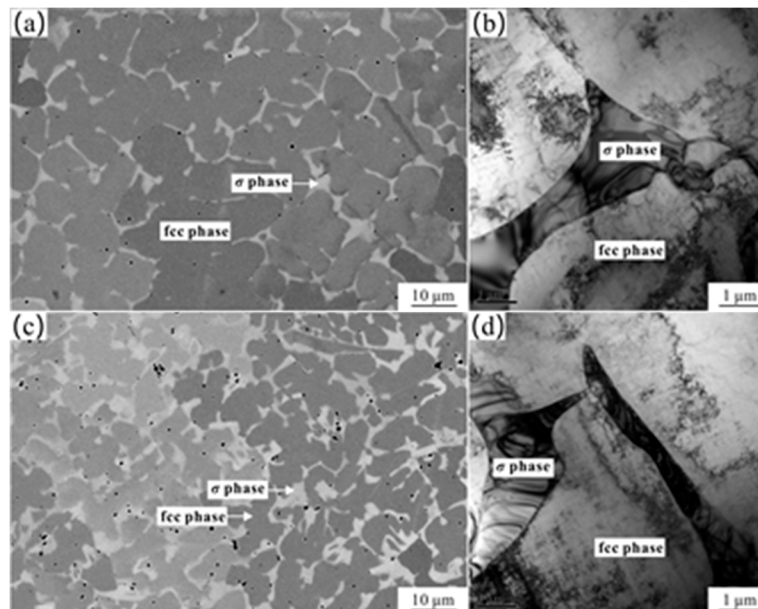


Figure 3. (a,c) SEM micrographs of the $V_{0.7}$ and $V_{0.8}$ alloys, showing the typical dendrite morphology. (b,d) TEM results of the $V_{0.7}$ and $V_{0.8}$ alloys, respectively. The black spots in (a,c) are the surface contaminants introduced during the polishing process.

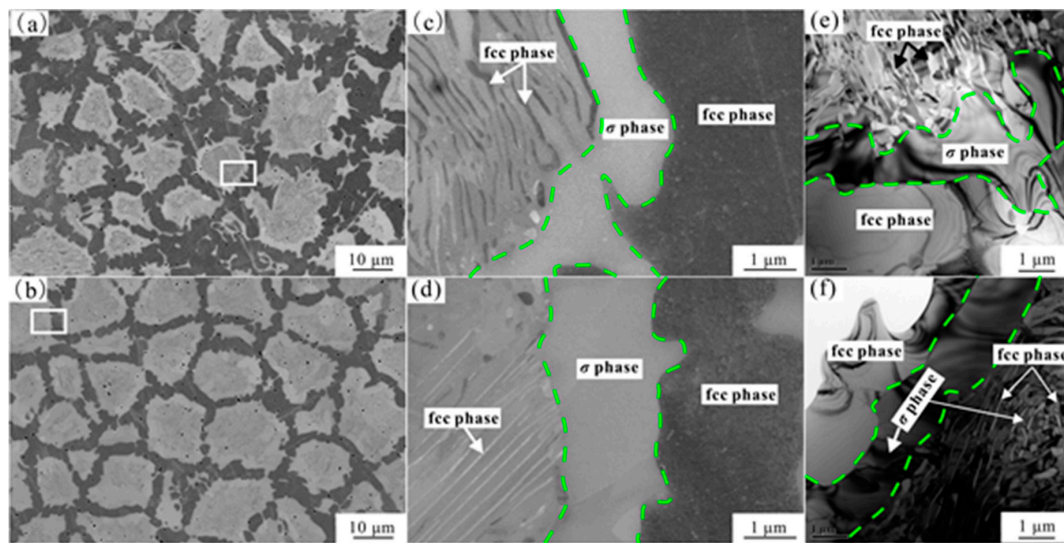


Figure 4. (a,b) SEM micrographs of the $V_{0.9}$ and $V_{1.0}$ alloys, respectively. (c,d) SEM micrographs at high magnification referring to the white rectangles in (a,b), respectively. (e,f) TEM results of the $V_{0.9}$ and $V_{1.0}$ alloys. The regions of the σ phase “shell” and interdendritic fcc phase are highlighted by green dashed lines. The black spots in (a,b) are the surface contaminants introduced during the polishing process.

However, the $V_{0.9}$ and $V_{1.0}$ alloys presented a typical equiaxed grain structure, with the grains being surrounded by a light-gray shell, as can be seen in Figure 4a,b. The detailed microstructure information was further studied by SEM at high magnification as well as TEM analysis (Figure 4c–f). The results showed that the matrix of the equiaxed grain was a continuous σ phase with the dispersion of fcc lamellae in the central region of the grain, presenting a typical core-shell structure. The interdendritic phase was proven to be a single fcc phase.

Figure 5 is the XRD diffraction patterns of the CoCrFeNiV_x alloys. It indicated that, for the alloys with a low concentration of V element ($x \leq 0.5$), it is mainly composed of the single fcc phase. For the alloys with $x \geq 0.7$, the σ phase with a tetragonal crystal structure was observed. This is consistent with the studies by Salishchev et al. [29], who also observed the existence of the σ phase in the as-solidified equal-atomic CoCrFeNiV HEA. Figure 5 shows that the peak intensity for the σ phase was enhanced along with the increase in the V concentration. Moreover, there was a significant shift of the diffraction peak of {111} crystal plane from 43.64° ($\text{CoCrFeNiV}_{0.25}$ alloy) to 43.50° (CoCrFeNi alloy), implying a lattice expansion of the fcc phase caused by the V element. In addition, the peak intensity of the {111} crystal plane of the fcc phase in the $V_{0.9}$ alloy was not the strongest one in the diffraction patterns, which might be due to the existence of the preferential grain orientation in the as-solidified bulk metallic materials [32]. In fact, the σ phase was formed first in the $V_{0.5}$ alloy, according to the microstructure presented in Figure 2. The deviation of phase identification by XRD analysis is due to the observed low fraction of the σ phase in the $V_{0.5}$ alloy.

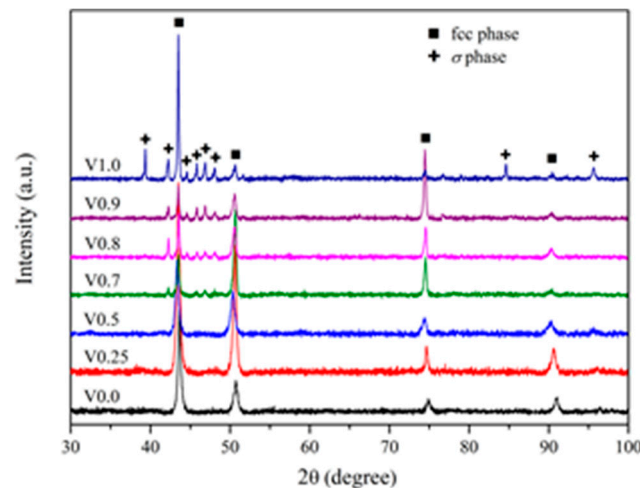


Figure 5. X-ray diffraction patterns of the studied high-entropy alloys with different V concentrations.

It is difficult to measure the cooling curves of the melt in the copper mold directly, which could be calibrated by means of indirect methods. Koziel [33] estimated the cooling rate of the melt experienced in the copper mold by using Fe-25 wt% Ni as the “standard thermometers”. The results indicated that for the \varnothing 5 mm casting rod, the minimum values of the superficial and axial cooling rates were about 1400 K s^{-1} and 11 K s^{-1} , respectively. Therefore, it could be accepted that, in the casting process, the melt in the center region of the mold experiences a certain undercooling, which can give access to a free growth of grains into the surrounding undercooled melt, usually resulting in the equiaxed microstructural morphology. Therefore, it seems acceptable that the $V_{0.9}$ and $V_{1.0}$ melts followed the described solidification path with the equiaxed crystal growth. A similar result was also observed in the copper-mold cast $\text{Al}_x\text{CoCrFeNiTi}$ HEAs, wherein large equiaxed grains solidified first from the melt and grew up [34]. However, it is rather difficult to understand the nature of the distinct core-shell structure. Previously, Ahamd et al. [35] investigated the undercooling behaviors on a Ni-25.3 at.% Si alloy (hypereutectic composition) using a melt-fluxing technique. They observed in the experiments that at all undercoolings, the melts were always solidified into a lamellar eutectic structure of single-phase $\gamma\text{-Ni}_{31}\text{Si}_{12}$ lamellae and a supersaturated Ni-rich phase, with the latter undergoing a eutectoid decomposition. The formation of the metastable phase was attributed to the possible low atomic mobility (sluggish diffusion), which was supported by the favorable experimental observations. Sluggish diffusion effect has long been treated as an intrinsic characteristic of the multi-component HEAs [11,36]. A number of recent studies [37–43] on both the solid and liquid state of the HEAs indicate the existence of the sluggish diffusion effect in HEAs. However, it can be influenced by the variation of the element component. As a result, the metastable phase might be retained easier in the as-solidified HEAs in comparison to that of the binary or ternary alloys (low-entropy alloy), according to the experimental evidences of the disordered bcc phase in the AlCoCrFeNi alloy [3] by traditional casting process ($45 \times 45 \times 10 \text{ mm}^3$) and the metastable phase in the Ni-25.3% Si and Ni-Fe-Si melts by severe non-equilibrium solidification processes [35,44,45].

By analogy, the observed duplex structure in the core region of the grain might be from the eutectoid decomposition of the unidentified metastable phase like a supersaturated solid solution. It is clear that this “eutectoid” structure does not fill the entire grain, with a thin layer of the single σ phase in the surface region of the grain. Considering that the σ phase is the continuous matrix phase, we may speculate that the elemental composition of the grain varies along the radial direction of the equiaxed grain during the solidification process due to the effect of the recalcence phenomenon. For further discussion, the elemental compositions of the local regions for the $V_{0.7}$, $V_{0.8}$, $V_{0.9}$, and $V_{1.0}$ alloys were also analyzed by EDX, as can be seen in Table 2. To obtain the average composition, the EDX measurement was repeated randomly at least 10 times for the fcc and σ phases in the $V_{0.7}$ and $V_{0.8}$ alloys, and at least five times for the core, shell, and interdendritic regions in the $V_{0.9}$ and $V_{1.0}$

alloys. It is clear that the composition of the fcc phase in the $V_{0.7}$ and $V_{0.8}$ alloys was quite close to the average composition of the corresponding alloys, which could be possible since the fcc phase is the primary phase solidified from the melt. The core region of the equiaxed grains contains a high composition of the Cr and Fe elements and a low composition of Co and Ni elements, in comparison to the average elemental composition of the $V_{0.9}$ alloy. The EDX results of the $V_{1.0}$ alloy also present a similar result, as shown in Table 2. Therefore, the origin of the core-shell equiaxed grain structure might be explained as follows. Initially, the undercooled melt facilitates the nucleation and subsequent growth of the unidentified metastable phase with a depletion of Cr and Ni elements in the surrounding areas. Grain growth is usually accompanied by the process of releasing latent heat, giving rise to continuous warming of the surrounding undercooled liquid. It might change the atomic diffusion behavior in the local region close to the solidified grain. In the early stage, a low fraction of solid phase, indicating low quantity of the released latent heat, will not give rise to a significant temperature increase of the surrounding melt. In this case, the atomic diffusion will not change too much and, therefore, the unidentified metastable phase could grow to a large size (Figure 5a,c). Then, as the fraction of the solid phase is increased, a high quantity of the latent heat would be expected and, in turn, the surrounding liquid could be heated to a high temperature, which can accelerate the atomic mobility and favor the formation of the thermodynamic equilibrium phase. Therefore, due to the available atomic diffusion rate in the “warm” melt, the surface region of the equiaxed grains and the interdendrite region solidified into the single σ and fcc phases, respectively. The elemental composition of the single σ phase was still close to that of the core region of the equiaxed grain. However, the obvious variation of the composition was observed in the fcc phase ($V_{0.9}$ and $V_{1.0}$ alloy) with a higher Ni composition, which is probably because of the enhanced atomic diffusion ability in the “warm” interdendritic melt. A similar result can be seen in the $V_{0.7}$ and $V_{0.8}$ alloys, namely that the σ phase in the interdendrite region, solidified in the final stage, possesses high compositions of Cr and V elements due to the sufficient diffusion time. The primary solidified unidentified metastable phase decomposes into the σ and fcc phases in the solidification process, with the presence of the eutectoid structure in the core region of the equiaxed grains.

Table 2. Average elemental composition of the CoCrFeNiV_x alloys measured by EDX.

	Alloy	Co/at.%	Cr/at.%	Fe/at.%	Ni/at.%	V/at.%
$V_{0.7}$	Matrix (fcc phase)	22.42 ± 0.22	20.75 ± 0.23	21.94 ± 0.49	21.23 ± 0.24	13.65 ± 0.52
	ID (σ phase)	20.02 ± 0.37	25.35 ± 0.52	20.51 ± 0.16	15.91 ± 0.57	18.23 ± 0.33
$V_{0.8}$	Matrix (fcc phase)	22.17 ± 0.15	19.79 ± 1.22	21.63 ± 0.24	21.26 ± 0.32	14.95 ± 0.24
	ID (σ phase)	20.07 ± 0.26	23.34 ± 0.80	20.42 ± 0.32	16.57 ± 0.17	19.30 ± 0.40
	ID (fcc phase)	22.00 ± 0.14	17.72 ± 0.16	19.99 ± 0.11	23.21 ± 0.13	17.08 ± 0.11
$V_{0.9}$	Shell (σ phase)	20.13 ± 0.22	22.76 ± 0.58	20.75 ± 0.25	16.91 ± 0.38	19.46 ± 0.37
	Core region	20.72 ± 0.26	21.93 ± 0.22	21.09 ± 0.21	18.02 ± 0.09	18.25 ± 0.26
	ID (fcc phase)	21.66 ± 0.16	16.69 ± 0.45	19.34 ± 0.36	23.71 ± 0.65	18.60 ± 0.27
$V_{1.0}$	Shell (σ phase)	19.99 ± 0.23	21.80 ± 0.24	20.30 ± 0.20	17.22 ± 0.29	20.69 ± 0.20
	Core region	20.37 ± 0.26	21.63 ± 0.23	20.79 ± 0.31	17.85 ± 0.13	19.36 ± 0.32

3.3. Mechanical Property

Figure 6 shows the compressive mechanical properties of CoCrFeNiV_x rods with different V content at a strain rate of $1.0 \times 10^{-3} \text{ s}^{-1}$. The results of the yield stress and fracture strength are given in Table 3. First, when $x \leq 0.5$, the $V_{0.0}$, $V_{0.25}$, and $V_{0.5}$ alloys were finally compressed into a drum shape without fracture, indicating an excellent ductility. The yield stress of the alloys, being at a low level, increased slightly from 164 MPa ($V_{0.0}$ alloy) to 291 MPa ($V_{0.5}$ alloy). This can be attributed to the solid solution strengthening, although the $V_{0.5}$ alloy contained a low fraction of the σ phase. A similar result was also observed by Gwalani et al. [22] in the compositionally graded AlCrFeMoV_x ($0 \leq x \leq 1$) high-entropy alloy fabricated by laser additive manufacturing. The addition of the V element does not change the phase constitution, but it results in the increase of the hardness from 485 HV to 581 HV. Meanwhile, as the V element was increased, the fraction of the second phase (σ

phase in the interdendritic region) increased. It is known that the σ phase, with a tetragonal crystal structure, was stronger than the fcc matrix phase due to the inherent characteristics of the crystal structure [46]. The enhanced yield stress of the $V_{0.7}$ and $V_{0.8}$ alloys, being about 392 MPa and 458 MPa, was due to the increasing fraction of the σ phase.

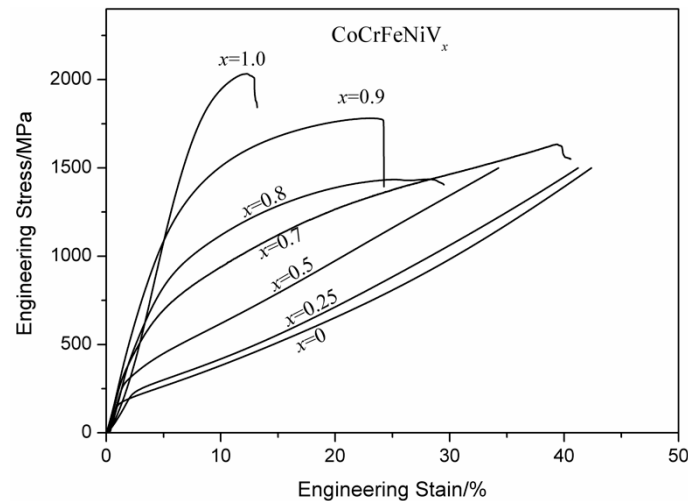


Figure 6. Compressive mechanical properties of the $CoCrFeNiV_x$ rods at room temperature.

The further increase of the mechanical properties was observed in the $V_{0.9}$ and $V_{1.0}$ alloys, with the yield strength being about 722 MPa and 1493 MPa, respectively. Generally, the precipitation of the additional phase could improve the strength first and then weaken the strength when its fraction exceeded a certain level, which can be worse if the additional phase is of a large size. Although the microstructure of the equiaxed grains in the $V_{0.9}$ and $V_{1.0}$ alloys was similar to a eutectic structure, the continuous matrix phase was the brittle σ phase. Therefore, to a certain degree, the microstructure of the $V_{0.9}$ and $V_{1.0}$ alloys could be treated as the hard particle reinforced HEA composite, resulting in a significant increase in the strength with a decrease in plasticity. A significant increase of the yield strength in the $V_{1.0}$ alloy, in comparison with that of the $V_{0.9}$ alloy, can be attributed to the higher fraction of the hard grains and the lower fraction of the fcc phase in the interdendrite region.

Table 3. The yield stress (σ_y) and fracture strength (σ_{max}) of the $CoCrFeNiV_x$ high-entropy alloys.

Alloy	σ_y /MPa	σ_{max} /MPa
$V_{0.0}$	164	-
$V_{0.25}$	234	-
$V_{0.5}$	291	-
$V_{0.7}$	392	1600
$V_{0.8}$	458	1435
$V_{0.9}$	722	1825
$V_{1.0}$	1493	2032

4. Conclusions

- (1) The addition of the V element facilitates the formation of the σ phase from the fcc matrix for the $CoCrFeNiV_x$ alloys, with a microstructure transition from a single fcc phase structure ($x \leq 0.25$) to a dendrite structure ($0.5 \leq x \leq 0.8$), and finally to the distinct equiaxed grain structure ($0.9 \leq x \leq 1.0$).
- (2) The formation of the σ phase can effectively enhance the mechanical properties of the alloys. As the V content increased, the yield strength of the alloys first increased gradually from 164 MPa ($x = 0$) to 458 MPa ($x = 0.8$), and then increased dramatically from 722 MPa ($x = 0.9$) to 1493 MPa ($x = 1.0$).

- (3) The core region of the equiaxed grain in the $V_{0.9}$ and $V_{1.0}$ alloys presents the fcc + σ eutectoid microstructure, which is derived from the eutectoid decomposition of the unidentified metastable phase.

Author Contributions: Conceptualization, L.C. and Y.C.; Funding acquisition, L.C. and Y.C.; Methodology, L.Z. (Lin Zhu), H.S. and Z.W.; Writing—original draft, L.C.; Writing—review & editing, L.C., Y.Y., Y.M., and L.Z. (Leilei Zhang).

Funding: This research was funded by the National Key R&D Program of China (2017YFB0703102), the Beijing Natural Science Foundation (2194074), the Science and Technology Project of Beijing Municipal Education Commission (KM201910009005), the Fundamental Scientific Research Funding of Beijing Municipal Education Commission (110052971921/040), the Yuqing Talent Support Program (18XN012-081), and the Undergraduate Scientific Research and Entrepreneurship Action Plan (18XN130) of North China University of Technology.

Acknowledgments: We would like to thank Fengbin Liu for his revision on the language.

Conflicts of Interest: The authors declare no conflict of interest.

References

1. He, J.Y.; Liu, W.H.; Wang, H.; Wu, Y.; Liu, X.J.; Nieh, T.G.; Lu, Z.P. Effects of Al addition on structural evolution and tensile properties of the FeCoNiCrMn high-entropy alloy system. *Acta Mater.* **2014**, *62*, 105–113. [[CrossRef](#)]
2. Li, X.; Lu, K. Playing with defects in metals. *Nature Mater.* **2017**, *16*, 700–701. [[CrossRef](#)]
3. Wang, W.R.; Wang, W.L.; Yeh, J.W. Phases, microstructure and mechanical properties of $Al_xCoCrFeNi$ high-entropy alloys at elevated temperatures. *J. Alloys Compd.* **2014**, *589*, 143–152. [[CrossRef](#)]
4. Cantor, B. Multicomponent and high entropy alloys. *Entropy* **2014**, *16*, 4749–4768. [[CrossRef](#)]
5. Shahmir, H.; Mousavi, T.; He, J.; Lu, Z.P.; Kawasaki, M.; Langdon, T.G. Microstructure and properties of a CoCrFeNiMn high-entropy alloy processed by equal-channel angular pressing. *Mater. Sci. Eng. A* **2017**, *705*, 411–419. [[CrossRef](#)]
6. Dong, Y.; Zhou, K.; Lu, Y.; Gao, X.; Wang, T.; Li, T. Effect of vanadium addition on the microstructure and properties of AlCoCrFeNi high entropy alloy. *Mater. Des.* **2014**, *57*, 67–72. [[CrossRef](#)]
7. Takeuchi, A.; Amiya, K.; Wada, T.; Yubuta, K.; Zhang, W. High-Entropy alloys with a hexagonal close-packed structure designed by equi-atomic alloy strategy and binary phase diagrams. *JOM* **2014**, *66*, 1984–1992. [[CrossRef](#)]
8. Cantor, B.; Chang, I.T.H.; Knight, P.; Vincent, A.J.B. Microstructural development in equiatomic multicomponent alloys. *Mater. Sci. Eng. A* **2004**, *375–377*, 213–218. [[CrossRef](#)]
9. Ranganathan, S. Alloyed pleasures: Multimetalllic cocktails. *Curr. Sci.* **2003**, *85*, 1404–1406.
10. Yeh, J.W.; Chen, S.K.; Lin, S.J.; Gan, J.Y.; Chin, T.S.; Shun, T.T.; Tsau, C.H.; Chang, S.Y. Nanostructured high-entropy alloys with multiple principal elements: Novel alloy design concepts and outcomes. *Adv. Eng. Mater.* **2004**, *6*, 299–303. [[CrossRef](#)]
11. Yeh, J.W. Recent progress in high-entropy alloys. *Eur. J. Control* **2006**, *31*, 633–648. [[CrossRef](#)]
12. Lin, C.M.; Tsai, H.L. Evolution of microstructure, hardness, and corrosion properties of high-entropy $Al_{0.5}CoCrFeNi$ alloy. *Intermetallics* **2011**, *19*, 288–294. [[CrossRef](#)]
13. Heczal, A.; Kawasaki, M.; Lábár, J.L.; Jang, J.; Langdon, T.G.; Gubicza, J. Defect structure and hardness in nanocrystalline CoCrFeMnNi high-entropy alloy processed by high-pressure torsion. *J. Alloys Compd.* **2017**, *711*, 143–154. [[CrossRef](#)]
14. Lu, Y.; Dong, Y.; Guo, S.; Jiang, L.; Kang, H.; Wang, T.; Wen, B.; Wang, Z.; Jie, J.; Cao, Z.; et al. A promising new class of high-temperature alloys: Eutectic high-entropy alloys. *Sci. Rep.* **2014**, *4*, 6200. [[CrossRef](#)] [[PubMed](#)]
15. He, J.Y.; Wang, H.; Huang, H.L.; Xu, X.D.; Chen, M.W.; Wu, Y.; Liu, X.J.; Nieh, T.G.; An, K.; Lu, Z.P. A precipitation-hardened high-entropy alloy with outstanding tensile properties. *Acta Mater.* **2016**, *102*, 187–196. [[CrossRef](#)]
16. Park, J.M.; Moon, J.; Bae, J.W.; Jung, J.; Lee, S.; Kim, H.S. Effect of annealing heat treatment on microstructural evolution and tensile behavior of $Al_{0.5}CoCrFeMnNi$ high-entropy alloy. *Mater. Sci. Eng. A* **2018**, *728*, 251–258. [[CrossRef](#)]

17. Gorr, B.; Azim, M.; Christ, H.J.; Mueller, T.; Schliephake, D.; Heilmaier, M. Phase equilibria, microstructure, and high temperature oxidation resistance of novel refractory high entropy alloys. *J. Alloys Compd.* **2015**, *624*, 270–278. [[CrossRef](#)]
18. Zhang, Y.; Zuo, T.T.; Cheng, Y.Q.; Liaw, P.K. High-entropy alloys with high saturation magnetization, electrical resistivity, and malleability. *Sci. Rep.* **2013**, *3*, 1455. [[CrossRef](#)]
19. Lu, Y.; Huang, H.; Gao, X.; Ren, C.; Gao, J.; Zhang, H.; Zheng, S.; Jin, Q.; Zhao, Y.; Lu, C.; et al. A promising new class of irradiation tolerant materials: Ti₂ZrHfV_{0.5}Mo_{0.2} high-entropy alloy. *J. Mater. Sci. Technol.* **2019**, *35*, 369–373. [[CrossRef](#)]
20. Wang, W.R.; Wang, W.L.; Wang, S.C.; Tsai, Y.C.; Lai, C.H.; Yeh, J.W. Effects of Al addition on the microstructure and mechanical property of Al_xCoCrFeNi high-entropy alloys. *Intermetallics* **2012**, *26*, 44–51. [[CrossRef](#)]
21. Banerjee, T.; Chaudhary, V.; Gwalani, B.; Choudhuri, D.; Mikler, C.V.; Soni, V.; Alam, T.; Ramanujan, R.V.; Banerjee, R. A combinatorial approach for assessing the magnetic properties of high entropy alloys: Role of Cr in AlCo_xCr_{1-x}FeNi. *Adv. Eng. Mater.* **2017**, *19*, 1700048.
22. Gwalani, B.; Soni, V.; Waseem, O.A.; Mantri, S.A.; Banerjee, R. Laser additive manufacturing of compositionally graded AlCrFeMoV_x (x = 0 to 1) high-entropy alloy system. *Optics Laser Technol.* **2019**, *113*, 330–337. [[CrossRef](#)]
23. Borkar, T.; Gwalani, B.; Choudhuri, D.; Mikler, C.V.; Yannetta, C.J.; Chen, X.; Ramanujan, R.V.; Styles, M.J.; Gibson, M.A.; Banerjee, R. A combinatorial assessment of Al_xCrCuFeNi₂ (0 < x < 1.5) complex concentrated alloys: Microstructure, microhardness, and magnetic properties. *Acta Mater.* **2016**, *116*, 63–76.
24. Gludovatz, B.; Hohenwarter, A.; Catoor, D.; Chang, E.H.; George, E.P.; Ritchie, R.O. A fracture-resistant high-entropy alloy for cryogenic applications. *Science* **2014**, *345*, 1153–1158. [[CrossRef](#)] [[PubMed](#)]
25. Zhang, J.Y.; Li, J.S.; Chen, Z.; Meng, Q.K.; Sun, F.; Shen, B.L. Microstructural evolution of a ductile metastable β titanium alloy with combined TRIP/TWIP effects. *J. Alloys Compd.* **2017**, *699*, 775–782. [[CrossRef](#)]
26. Wu, Y.; Ma, D.; Li, Q.K.; Stoica, A.D.; Song, W.L.; Wang, H.; Liu, X.J.; Stoica, G.M.; Wang, G.Y.; An, K.; et al. Transformation-induced plasticity in bulk metallic glass composites evidenced by in-situ neutron diffraction. *Acta Mater.* **2017**, *124*, 478–488. [[CrossRef](#)]
27. Li, Z.; Pradeep, K.G.; Deng, Y.; Raabe, D.; Tasan, C.C. Metastable high-entropy dual-phase alloys overcome the strength-ductility trade-off. *Nature* **2016**, *534*, 227–231. [[CrossRef](#)]
28. Huang, H.; Wu, Y.; He, J.; Wang, H.; Liu, X.; Wu, W.; Lu, Z.P. Phase-transformation ductilization of Brittle high-entropy alloys via metastability engineering. *Adv. Mater.* **2017**, *29*, 1701678. [[CrossRef](#)]
29. Salishchev, G.A.; Tikhonovsky, M.A.; Shaysultanov, D.G.; Stepanov, N.D.; Kuznetsov, A.V.; Kolodiy, I.V.; Tortika, A.S.; Senkov, O.N. Effect of Mn and V on structure and mechanical properties of high-entropy alloys based on CoCrFeNi system. *J. Alloys Compd.* **2014**, *591*, 11–21. [[CrossRef](#)]
30. Li, J.; Jia, W.; Wang, J.; Kou, H.; Zhang, D.; Beaugnon, E. Enhanced mechanical properties of a CoCrFeNi high entropy alloy by supercooling method. *Mater. Des.* **2016**, *95*, 183–187. [[CrossRef](#)]
31. Bazlov, A.I.; Churyumov, A.Y.; Louzguine-luzgin, D.V. Investigation of the structure and properties of the Fe-Ni-Co-Cu-V multiprincipal element alloys. *Metall. Mater. Trans. A* **2018**, *49*, 5646–5652. [[CrossRef](#)]
32. Ahmad, R.; Cochrane, R.F.; Mullis, A.M. Disorder trapping during the solidification of βNi₃Ge from its deeply undercooled melt. *J. Mater. Sci.* **2012**, *47*, 2411–2420. [[CrossRef](#)]
33. Kozieł, T. Estimation of cooling rates in suction casting and copper-mould casting processes. *Arch. Metall Mater.* **2015**, *60*, 767–771. [[CrossRef](#)]
34. Lindner, T.; Löbel, M.; Mehner, T.; Dietrich, D.; Lampke, T. The phase composition and microstructure of Al_xCoCrFeNiTi alloys for the development of high-entropy alloy systems. *Metals* **2017**, *7*, 162. [[CrossRef](#)]
35. Ahmad, R.; Cochrane, R.F.; Mullis, A.M. The formation of regular α Ni-γ (Ni₃₁Si₁₂) eutectic structures from undercooled Ni-25 at.% Si melts. *Intermetallics* **2012**, *22*, 55–61. [[CrossRef](#)]
36. Tsai, M.H.; Yeh, J.W. High-entropy alloys: A critical review. *Mater. Res. Lett.* **2014**, *2*, 107–123. [[CrossRef](#)]
37. Tsai, K.Y.; Tsai, M.H.; Yeh, J.W. Sluggish diffusion in Co-Cr-Fe-Mn-Ni high entropy alloys. *Acta Mater.* **2013**, *61*, 4887–4897. [[CrossRef](#)]
38. Li, Q.; Chen, W.; Zhong, J.; Zhang, L.; Chen, Q.; Liu, Z.K. On sluggish diffusion in fcc Al-Co-Cr-Fe-Ni high-entropy alloys: An experimental and numerical study. *Metals* **2017**, *8*, 16. [[CrossRef](#)]
39. Tan, Y.; Li, J.; Wang, J.; Kou, H. Seaweed eutectic-dendritic solidification pattern in a CoCrFeNiMnPd eutectic high-entropy alloy. *Intermetallics* **2017**, *85*, 74–79. [[CrossRef](#)]
40. Chen, C.; Wong, K.; Krishnan, R.P.; Embs, J.P.; Chathoth, S.M. A slow atomic diffusion process in high-entropy glass-forming metallic melts. *J. Phys. D: Appl. Phys.* **2018**, *51*, 145301. [[CrossRef](#)]

41. Divinski, S.V.; Pokoev, A.V.; Esakkiraja, N.; Paul, A. A mystery of “sluggish diffusion” in high-entropy alloys: The truth or a myth? *Diffus. Found.* **2018**, *17*, 69–104. [[CrossRef](#)]
42. Osetsky, Y.N.; Beland, L.K.; Barashev, A.V.; Zhang, Y. On the existence and origin of sluggish diffusion in chemically disordered concentrated alloys. *Curr. Opin. Solid State Mater. Sci.* **2018**, *22*, 65–74. [[CrossRef](#)]
43. Wang, R.; Chen, W.; Zhong, J.; Zhang, L. Experimental and numerical studies on the sluggish diffusion in face centered cubic Co-Cr-Cu-Fe-Ni high-entropy alloys. *J. Mater. Sci. Technol.* **2018**, *34*, 1791–1798. [[CrossRef](#)]
44. Cao, L.; Cochrane, R.F.; Mullis, A.M. Solidification morphology and phase selection in drop-tube processed Ni-Fe-Si intermetallics. *Intermetallics* **2015**, *60*, 33–44. [[CrossRef](#)]
45. Cao, L.; Cochrane, R.F.; Mullis, A.M. Microstructure evolution and phase formation in rapidly solidified Ni-25.3 at. pct Si alloy. *Metall. Mater. Trans. A* **2015**, *46*, 2015–4705. [[CrossRef](#)]
46. Tung, C.C.; Yeh, J.W.; Shun, T.; Chen, S.K.; Huang, Y.S.; Chen, H.C. On the elemental effect of AlCoCrCuFeNi high-entropy alloy system. *Mater. Lett.* **2007**, *61*, 1–5. [[CrossRef](#)]



© 2019 by the authors. Licensee MDPI, Basel, Switzerland. This article is an open access article distributed under the terms and conditions of the Creative Commons Attribution (CC BY) license (<http://creativecommons.org/licenses/by/4.0/>).